Contents lists available at ScienceDirect

Remote Sensing of Environment

journal homepage: www.elsevier.com/locate/rse

Unravelling a large methane emission discrepancy in Mexico using satellite observations

Lu Shen [a,b,*], Daniel Zavala-Araiza [b,f], Ritesh Gautam [b,**], Mark Omara [b], Tia Scarpelli [a],
Jianxiong Sheng [c], Melissa P. Sulprizio [a], Jiawei Zhuang [a], Yuzhong Zhang [d,e], Zhen Qu [a],
Xiao Lu [a], Steven P. Hamburg [b], Daniel J. Jacob [a]

[a] School of Engineering and Applied Sciences, Harvard University, Cambridge, MA 02138, United States
[b] Environmental Defense Fund, Washington, DC 20009, United States
[c] Center for Global Change Science, Massachusetts Institute of Technology, Cambridge, MA 02139, United States
[d] Key Laboratory of Coastal Environment and Resources of Zhejiang Province (KLaCER), School of Engineering, Westlake University, Hangzhou, Zhejiang, China
[e] Institute of Advanced Technology, Westlake Institute for Advanced Study, Hangzhou, Zhejiang, China
[f] Institute for Marine and Atmospheric Research Utrecht, Utrecht University, 3584, CC, Utrecht, the Netherlands

ABSTRACT

We use satellite observations from the Tropospheric Monitoring Instrument (TROPOMI) to map and quantify methane emissions from eastern Mexico using an atmospheric inverse analysis. Eastern Mexico covers the vast majority of the national oil and gas production. Using TROPOMI measurements from May 2018 to December 2019, our methane emission estimates for eastern Mexico are 5.0 ± 0.2 Tg a^{-1} for anthropogenic sources and 1.5 ± 0.1 Tg a^{-1} for natural sources, representing 45% and 34% higher annual methane fluxes respectively compared to the most recent estimates based on the Mexican national greenhouse gas inventory. Our results show that Mexico's oil and gas sector has the largest discrepancy, with oil and gas emissions (1.3 ± 0.2 Tg a^{-1}) higher by a factor of two relative to bottom-up estimates—accounting for a quarter of total anthropogenic emissions. Our satellite-based inverse modeling estimates show that more than half of the oil/gas emissions in eastern Mexico are from the southern onshore basin (0.79 ± 0.13 Tg a^{-1}), pointing at high emission sources which are not represented in current bottom-up inventories (e.g., venting of associated gas, high-emitting gathering/processing facilities related to the transport of associated gas from offshore). These findings suggest that stronger mitigation measures are critical to curbing the anthropogenic footprint of methane emissions in Mexico, especially the large contribution from the oil and gas sector.

1. Introduction

Methane is the second most important anthropogenic greenhouse gas and impacts the climate on a decadal time scale (IPCC, 2013). Methane emissions from human activities have led to 0.97 Wm^{-2} of radiative forcing since preindustrial times, compared to 1.7 Wm^{-2} from carbon dioxide (Myhre et al., 2013). According to recent estimates, Mexico emits ~2% of global anthropogenic methane (Crippa et al., 2019) and of that 15% of anthropogenic methane emissions are from the oil/gas sector (Scarpelli et al., 2020). Methane emissions in Mexico are subject to large uncertainties (e.g. Scarpelli et al., 2020; Sheng et al., 2017) including the relative sectoral contributions to the national total.

Existing bottom-up inventories estimate 4–7 Tg a^{-1} for anthropogenic emissions and 0.8–3.6 Tg a^{-1} for the oil/gas sector (Janssens-Maenhout et al., 2019; Scarpelli et al., 2020; Sheng et al., 2017; SEMARNAT, 2012; IMP, 2012; INECC and SEMARNAT, 2018). In the case of emissions from oil and gas sources, these inventories are largely based on emission factors generated by other countries, and not based on local measurements (INECC and SEMARNAT, 2018), thus—increasing the uncertainty in the magnitude of emissions and making effective mitigation action more challenging.

Recently, Mexico indicated plans to reduce oil and gas related methane emissions by 40–45% by year 2025 relative to the 2012 levels (https://pm.gc.ca/en/news/statements/2016/06/29/leaders-state

---

ment-north-american-climate-clean-energy-and-environment, accessed in October 2020). To support this emissions reduction target, the federal government published in 2018 a set of regulations that require each operating facility to report current emissions and develop emission reduction plans implementing a set of technical standards (e.g., use of zero bleed equipment, deployment of a system of frequent leak detection and repair activities) (https://www.dof.gob.mx/nota_detalle.php?codigo=5543033&fecha=06/11/2018, accessed in October 2020). For these mitigation policies to be effective—and to evaluate their outcomes— it becomes critical to quantify the current magnitude of emissions as well as the spatial distribution of key sources. Here, we use satellite observations aided by atmospheric inverse modeling to characterize methane emissions in eastern Mexico (east of 104°W), a region that is estimated to account for 70% of Mexico's anthropogenic emissions, 99% of oil/gas production, and 95% of oil/gas related methane emissions, according to Scarpelli et al. (2020).

Using aircraft measurements, Zavala-Araiza et al. (2020) found that methane emissions from offshore oil and gas platforms in Mexican waters are >10 times lower than the Mexican national greenhouse gas inventory estimate. In contrast, they also found that emissions for a key onshore production region are >10 times higher. Although field campaigns can provide in-depth information, they are typically limited in their spatial extent and temporal duration. The space-borne Tropospheric Monitoring Instrument (TROPOMI) provides a novel opportunity to map the atmospheric methane enhancements in Mexico. Previous studies have demonstrated that TROPOMI can be used in the detection and quantification of methane emissions from large point and area sources (Varon et al., 2019; Pandey et al., 2019; Zhang et al., 2020; de Gouw et al., 2020; Schneising et al., 2020). In this study, we characterize anthropogenic methane emissions from eastern Mexico and demonstrate the effectiveness of a new emerging paradigm of the application of satellite observations in quantifying emissions from individual source sectors, with particular focus on the oil/gas sector.

2. Data and methods

2.1. Satellite observations

We use the column-averaged dry air methane ratios (XCH_4) retrieved from TROPOMI measurements after accounting for the surface albedo effect (Hasekamp et al., 2019) from May 2018 to December 2019 for the atmospheric inverse analysis. TROPOMI was launched in October 2017 and the operational data stream started in May 2018. It is onboard the polar sun-synchronous Sentinel-5 Precursor satellite with a ∼ 13:30 local overpass time and provides daily global coverage in cloud-free conditions with 7 km × 7 km spatial resolution at nadir (Hu et al., 2016; Veefkind et al., 2012). The spatial resolution increased to 7 km × 5.5 km at nadir after August 2019. The XCH_4 retrieval uses the 2.3 μm methane absorption band in the short-wave infrared (SWIR) and has near-unit sensitivity down to the surface. Only the recommended higher-quality XCH_4 measurements are used (Hasekamp et al., 2019) in this study (qa_value >0.5). The TROPOMI XCH_4 product has a global mean bias of 3–4 ppbv when validated with independent ground-based measurements from the Total Column Carbon Observing Network (TCCON) (Hasekamp et al., 2019; Lorente et al., 2020). When mapped to 0.1° × 0.1° horizontal resolution, TROPOMI coverage for May 2018 – December 2019 includes >100 days of successful observations in northwestern Mexico and 40–60 days along the east coast (Fig. S1). The glint ocean observations are not retrieved at this time from TROPOMI so there are no observations over the offshore regions of Mexico. We also use the 2018–2019 dry column methane mixing ratios from Greenhouse Gases Observing Satellite (GOSAT version 9.0, Butz et al., 2011; Parker et al., 2020) to intercompare with TROPOMI XCH_4 retrievals. The comparisons show that the correlation coefficient between TROPOMI and GOSAT is 0.63 (Fig. S2a). TROPOMI data are lower than GOSAT by 3.9 ppb in eastern Mexico and southern US (Fig. S2), and this bias is independent of the SWIR albedo (Fig. S3).

We also use TROPOMI data for the tropospheric column density of NO_2 with a spatial resolution of 7 km × 3.5 km at nadir for the same time period as the methane analysis, and the gas flaring radiant heat data (radiant temperature of 1400–2500 K for flaring detections) from the Visible Infrared Imaging Radiometer Suite (VIIRS) instrument onboard the Suomi National Polar-Orbiting Partnership satellite with a spatial resolution of 750 m × 750 m (Elvidge et al., 2016).

2.2. GEOS-Chem flexgrid simulations and prior estimates

We use GEOS-Chem 12.7.0 (doi:https://doi.org/10.5281/zenodo.1343546) as the forward model to simulate the distribution of atmospheric methane and construct the sensitivity matrix of concentrations to the perturbation of emissions (Jacobian matrix) in the analytical inverse analysis. The model is driven by GEOS-FP reanalysis meteorological fields from NASA Global Modeling and Assimilation Office (GMAO, Lucchesi, 2013). We use a nested version of GEOS-Chem with 0.25° × 0.3125° horizontal resolution including 1199 grid cells in eastern Mexico (104°W-85°W, 14°N-32°N) (Fig. S4a). We use boundary conditions from a 4° × 5° global simulation. We calculate a scaling factor for all pairs of GEOS-Chem outputs and TROPOMI data within 1000 km and 15 days for each gridcell and timestep, and then we apply this scaling factor to correct any bias in the boundary conditions of GEOS-Chem. To better account for the transport, we enlarge the simulation domain by 4° (108°W-81°W, 10°N-36°N) in four directions, as shown in Fig. S4b. We aggregate these gridcells outside eastern Mexico into 8 clusters using the k-means algorithm based on the center longitudes and latitudes of each gridcell (Fig. S4b). We also optimize the emissions of these 8 clusters in order to further correct boundary conditions but only report emissions for the eastern Mexico domain. Taken together, the state vector in our inverse analysis consists of 1199 native gridcells in eastern Mexico and 8 clusters in the surrounding region (Fig. 1 and S4).

An essential component of inverse analyses is the choice of a bottom-up inventory as a prior estimate. We use the 0.1°x0.1° anthropogenic emissions inventory for Mexico from Scarpelli et al. (2020), which is constructed by spatially allocating national emission estimates from the National Inventory of Greenhouse Gases and Compounds constructed by the Instituto Nacional de Ecología y Cambio Climático (INECC) with detailed sectorial breakdown (INECC and SEMARNAT, 2018). For the oil/gas sector, the emissions are allocated to different gridcells on the basis of production which does not necessarily correlate with emissions. Even though the oil and gas production in Mexico has decreased by 20–30% from 2015 to 2019 (Zavala-Araiza et al., 2020), the spatial distribution of oil and gas production remain unchanged (Fig. S5). Since there are no TROPOMI XCH_4 retrievals over the offshore regions, we correct the emissions there based on aircraft measurements from Zavala-Araiza et al. (2020), which suggested that the bottom-up inventory in the offshore regions need to be decreased by 90%. Therefore, we apply a scaling factor of 0.1 to emissions from the oil/gas sector there, which leads to a decrease of 0.23 Tg a^{-1} in national oil and gas emissions. Prior anthropogenic emissions for the inversion are thus 3.4 Tg a^{-1} in eastern Mexico (70% of national total), with major contributors from livestock (1.40 Tg a^{-1}, 60% of national sector total), landfills (0.61 Tg a^{-1}, 75%), oil and gas (0.55 Tg a^{-1}, 96%), waste (0.53 Tg a^{-1}, 72%), coal mining (0.24 Tg a^{-1}, 88%), and anthropogenic biomass burning (0.02 Tg a^{-1}, 79%). Natural emissions are 1.1 Tg a^{-1} in total in eastern Mexico, mainly from wetlands as given by the mean of the WetCHARTS inventory ensemble (Bloom et al., 2017). Taken together, the total prior methane emissions in eastern Mexico is 4.5 Tg a^{-1}. Fig. S6 shows the distribution of these prior methane emissions over eastern Mexico. Further investigation suggests that the model bias relative to TROPOMI is independent of the SWIR albedo (Fig. S7).

We test the robustness of our inverse analysis by a series of sensitivity calculations involving perturbations to the prior inventory for the oil/gas sector. Zavala-Araiza et al. (2020) hypothesized that the transport of
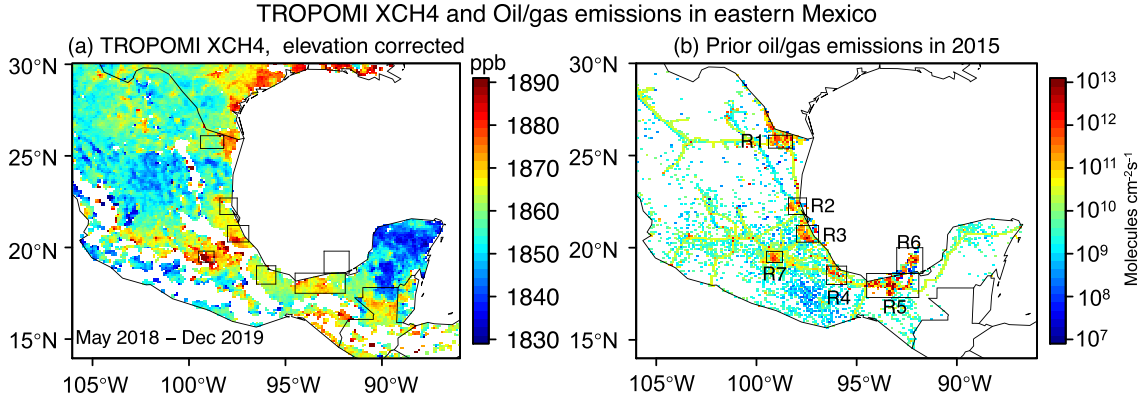
TROPOMI XCH4 and Oil/gas emissions in eastern Mexico

Fig. 1. TROPOMI column methane and oil/gas sectoral bottom-up emissions in eastern Mexico (106°W-86°W, 14°N-30°N). (a) TROPOMI satellite observations (May 2018 – December 2019), mapped to 0.1°x0.1° resolution and corrected for surface topography as 7 ppb/km (Kort et al., 2014; Zhang et al., 2020). This altitude correction is for visual purposes only; the actual inversion uses the uncorrected TROPOMI data since the forward model accounts for surface topography. White areas have no observations (ocean, mountains). (b) Bottom-up emissions from the oil/gas sector in eastern Mexico from Scarpelli et al. (2020) for 2015 with 0.1°x0.1° resolution, and including downward correction to offshore oil/gas emissions (see text). Seven regions (R1-R7) with high emissions are defined by rectangles in both panels.

offshore associated gas to onshore infrastructure may be leading higher emissions from the onshore gathering and processing facilities. Here we not only decrease the offshore emissions by 90% but also redistribute these emissions to inland gridcells. More specifically, our base inversion apply a scaling factor of 0.1 to offshore gridcells; our perturbations of oil/gas sources in prior inventory include (1) applying a scaling factor of 0.1 to offshore gridcells (R6, see Fig. 1 for the definition of these domains) but 1.5 to all other gridcells in eastern Mexico, and (2) applying a scaling factor of 0.1 to offshore gridcells (R6) but 2.0 to onshore gridcells (R5). These scaling factors applied here are based on the bottom-up inventory of Scarpelli et al. (2020) and the total emissions from the oil/gas sector are the same (0.78 Tg a^{-1}) for these two variants of prior.

2.3. Atmospheric inverse analysis

We solve for the posterior estimates of spatially resolved methane emissions in eastern Mexico using Bayesian inverse analysis of methane observations from TROPOMI. The cost function J of this problem can be described as:

$$J(x) = (x - x_A)^T S_A^{-1}(x - x_A) + \gamma (y - Kx)^T S_O^{-1}(y - Kx) \tag{E1}$$

Where x is the state vector, x_A is the prior estimates of emissions, K is the Jacobian matrix describing the sensitivity of column-averaged concentrations to the perturbation of emissions in each gridcell, y is the methane observations from TROPOMI measurements, S_A and S_O are covariance matrices for prior and observational errors, and γ is an additional regularization factor (Brasseur and Jacob, 2017). We construct the observational error covariance matrix S_O by applying the residual error method, which assumes that the statistics of residual error (after removing the mean bias) between the observations and a GEOS-Chem simulation with prior emissions defines the observational error variance (Heald et al., 2004; Wecht et al., 2014). The resulting average observational error standard deviation in eastern Mexico is 15 ppb. We assume 50% error standard deviation for all anthropogenic and natural emissions on the 0.25°x0.3125° grid and also for the 8 clusters in the surrounding regions, with no spatial error covariance, as recommended by Scarpelli et al. (2020). We account for the covariant structure of the observational error through the regularization term γ in the inversion (Brasseur and Jacob, 2017; Maasakkers et al., 2019).

The analytical solution for $\nabla_x J(x) = 0$ yields the optimal estimate $\hat{x}$, the posterior error covariance matrix $\hat{S}$, and the averaging kernel matrix A as follows:

$$\hat{x} = x_A + (\gamma K^T S_O^{-1} K + S_A^{-1})^{-1} \gamma K^T S_O^{-1}(y - Kx) \tag{E2}$$

$$\hat{S}^{-1} = \gamma K^T S_O^{-1} K + S_A^{-1} \tag{E3}$$

$$A = I_n - \hat{S} S_A^{-1} \tag{E4}$$

where I_n is the identity matrix. The averaging kernel matrix A defines the sensitivity of the posterior solution to the true state. The trace of A quantifies the degrees of freedoms for signal (DOFS), representing the number of independent pieces of information that can be effectively optimized in the inversion. We construct the Jacobian matrix K by perturbing each element of the state vector independently. The state vector has a dimension of 1207, including 1199 native grid cells in eastern Mexico and 8 abutting grid cell clusters (Fig. S4).

We generally find that different emission sectors have different spatial error correlations. The error covariance is significant at the regional scale for wetland (Bloom et al., 2017) but quickly decays for anthropogenic sectors when the distance is greater than 0.5° (Maasakkers et al., 2016). Since we focus on anthropogenic emissions in this study, we take the observational error S_O as diagonal and use γ to account for missing covariant structure, particularly when there is more than one observation per model grid cell on a given day. γ is 1 only if all observations are independent. We determine the optimal regularization parameter γ based on the L-curve plot (Fig. S8) (Maasakkers et al., 2019). We choose γ to be 0.25, and also examine the sensitivity of our inverse results to the choice of γ by conducting sensitivity inversions with γ as 0.1 and 0.5.

Throughout this study, we report the one standard deviation error of satellite derived emissions by including (i) the posterior error, (ii) the uncertainty of using three different priors, and (iii) the three different weighting of observations (γ) through bootstrapping.

2.4. Posterior correction factor for each sector

Each grid cell consists of emissions from different sectors with different prior error standard deviations. Using one gridcell k with M different source sectors as the example, here we demonstrate how we calculate the posterior correction factor f_i ($1 \leq i \leq M$) for each sector. We apply 50% error standard deviation to prior estimates for each gridcell (Scarpelli et al., 2020) and calculate the posterior correction factor f_0 ($f_0 = \frac{\hat{x}_k}{x_{A,k}}$) from E2 for this gridcell k.

$$\sum_{i=1}^{M} \alpha_i f_i = f_0 \tag{E5}$$

$$\sum_{i=1}^{M} \alpha_i = 1 \tag{E6}$$

Where α_i is the fraction of emissions of each sector taken from the prior and f_i is the posterior correction factor for i^{th} sector in this gridcell. Here we assume that f_i follows the Gaussian distribution of N(1, σ_i), where σ_i is the error standard deviation on the prior estimate for that sector. The cost function Z to optimize for the correction factor for each source sector can be written as:

$$Z = \sum_{i=1}^{M} \frac{(f_i - 1)^2}{\sigma_i^2} \tag{E7}$$

To solve for the minimum of E7, we use the Cauchy–Schwarz inequality, which can be written as:

$$\sum_{i=1}^{M} \frac{(f_i - 1)^2}{\sigma_i^2} \sum_{i=1}^{M} \alpha_i^2 \sigma_i^2 \geq \left(\sum_{i=1}^{M} \alpha_i (f_i - 1) \right)^2 = (f_0 - 1)^2 \tag{E8}$$

The equality holds when there exists a nonzero constant β such that for all $1 \leq i \leq M$,

$$f_i - 1 = \beta \alpha_i \sigma_i^2 \tag{E9}$$

Where β can be written as:

$$\beta = \frac{f_0 - 1}{\sum_{i=1}^{M} \alpha_i^2 \sigma_i^2} = \frac{f_0 - 1}{\sigma_0^2} \tag{E10}$$

Where σ_0 is the prior error standard deviation for each grid cell and it is 50% in our case. So each f_i can be written as:

$$f_i = \beta \alpha_i \sigma_i^2 + 1 \tag{E11}$$

We assume that the local uncertainty from each sector is proportional to the reported national uncertainty. Scarpelli et al. (2020) found that the national sector uncertainties reported by INECC are relatively large for fuel sectors but anomalously small for the other major sub-sectors in Mexico. So we use the uncertainties from the U.S. gridded inventory (Maasakkers et al., 2016), which has similar uncertainties for fuel sectors but larger uncertainties for other anthropogenic sectors. More specifically, we use a local error standard deviation for each sector scaled to national totals of 20% for oil/gas, 7% for coal, 26% for landfill, 8% for livestock, 10% for wastewater, 9% for rice, and 53% for biomass burning; we also use 70% for wetland (Bloom et al., 2017) and 25% for all other sources. As part of this study, we will also test the sensitivity of our results to these national errors by assuming they have another 25% uncertainty. The local scaling factor η for the error variance of each sector relative to the national total is given by:

$$\eta = \frac{\sigma_0^2}{\sum_{i=1}^{M} \alpha_i^2 \sigma_{i,nation}^2} \tag{E12}$$

So that

$$\sigma_i = \sqrt{\eta} \sigma_{i,nation} \tag{E13}$$

where the '*nation*' index refers to the error standard deviations on the national totals. In this manner, the local error variances for the different sectors add up to the total prior error variance ($\sigma_0^2 = 0.25$, corresponding to $\sigma_0 = 50\%$). Thus the local posterior correction factor for each sector is:

$$f_i = \frac{\eta \alpha_i \sigma_{i,nation}^2 (f_0 - 1)}{\sigma_0^2} + 1 \ (1 \leq i \leq M) \tag{E13}$$

3. Results

3.1. Satellite observations and prior estimates

Fig. 1A shows the spatial distribution of 2018–2019 averaged TROPOMI column-averaged methane mixing ratio over eastern Mexico. The data are corrected for topography following Kort et al. (2014) and Zhang et al. (2020) for visual clarity, but this correction is not used in the inverse analysis because the GEOS-Chem forward model accounts for topography. Substantial enhancements of XCH$_4$ above the topographic mean are found along the eastern coastal areas and in Mexico City. Fig. 1B displays the prior estimates of oil/gas emissions used in this study. It features 7 subdomains (R1-R7) that in total account for ~70% of national oil/gas emissions. The spatial distributions of TROPOMI XCH$_4$ and oil/gas emissions generally show close association in eastern Mexico.

Fig. 2a-b shows high oil/gas production along the coastal basins (R1-R6) and not in Mexico City (R7). Methane emissions in Mexico City are mainly from natural gas utilization (natural gas distribution and end use) and other sectors such as wastewater and landfills. Several of the production hotspots coincide with the dominant oil production infrastructure, with the exception of the northernmost hotspot (R1) with intensive gas production but near-zero oil production. Regions R1-R6 account for 98% of national oil and 90% of national gas production (Table S1).

We also analyze plausible associations between oil/gas production and methane emissions with oil/gas combustion related sources including flaring. Flares are used to burn unwanted natural gas during oil exploration and production of oil/gas, particularly common in oil production basins where co-produced associated gas is not effectively captured and processed. Data from the Visible Infrared Imaging Radiometer Suite (VIIRS) shows high flaring intensity in oil/gas production regions R2-R6 (Fig. 2c), which are associated with high oil production (Fig. 2a-b, Table S1). We also examine NO$_2$ over these onshore production areas, as previous work found enhanced NO$_2$ concentrations attributable to gas flaring and other combustion activities in the US and offshore Mexico (e.g. Zhang et al., 2019; Duncan et al., 2016). The TROPOMI observations show enhanced NO$_2$ concentrations in oil/gas producing basins R2-R6, where flaring seems prevalent. High NO$_2$ is also observed in Mexico City, where it can be attributed to other anthropogenic sources such as power plants and transportation in this urban area (Smith et al., 2018). We do not observe significant flaring heat (Fig. 2c) or elevated NO$_2$ concentrations in R1 (Fig. 2d), as it is dominated by gas production and little oil production, and flaring is not likely a major source of emissions there (Fig. a-b, Table S1). This observation of a close association between co-occurring enhancements in methane and NO$_2$, and flaring in oil producing basins was also observed in the Permian Basin in the US (de Gouw et al., 2020; Zhang et al., 2020) and was previously explored by Zhang et al. (2019) for Mexican offshore production.

3.2. Inverse analysis

We quantify the emissions in eastern Mexico using TROPOMI measurements through an atmospheric inverse analysis. Fig. 3 shows the results of the inversion including the optimized posterior correction factors and the averaging kernel sensitivities. Our results show that we need to apply a posterior correction factor of 1.5–2.5 to Mexico City and onshore coastal areas (Fig. 3a), where in the case of the latter oil/gas related methane emissions are concentrated and dense oil/gas activity is co-located. The inversion is able to constrain about 33 pieces of independent information in the spatial distribution of methane emissions as measured by the averaging kernel matrix. The highest sensitivity is also found in these coastal oil/gas production regions and Mexico City (Fig. 3b), indicating TROPOMI data can provide better constraints there due to greater number of satellite observations (Fig. S1) and higher
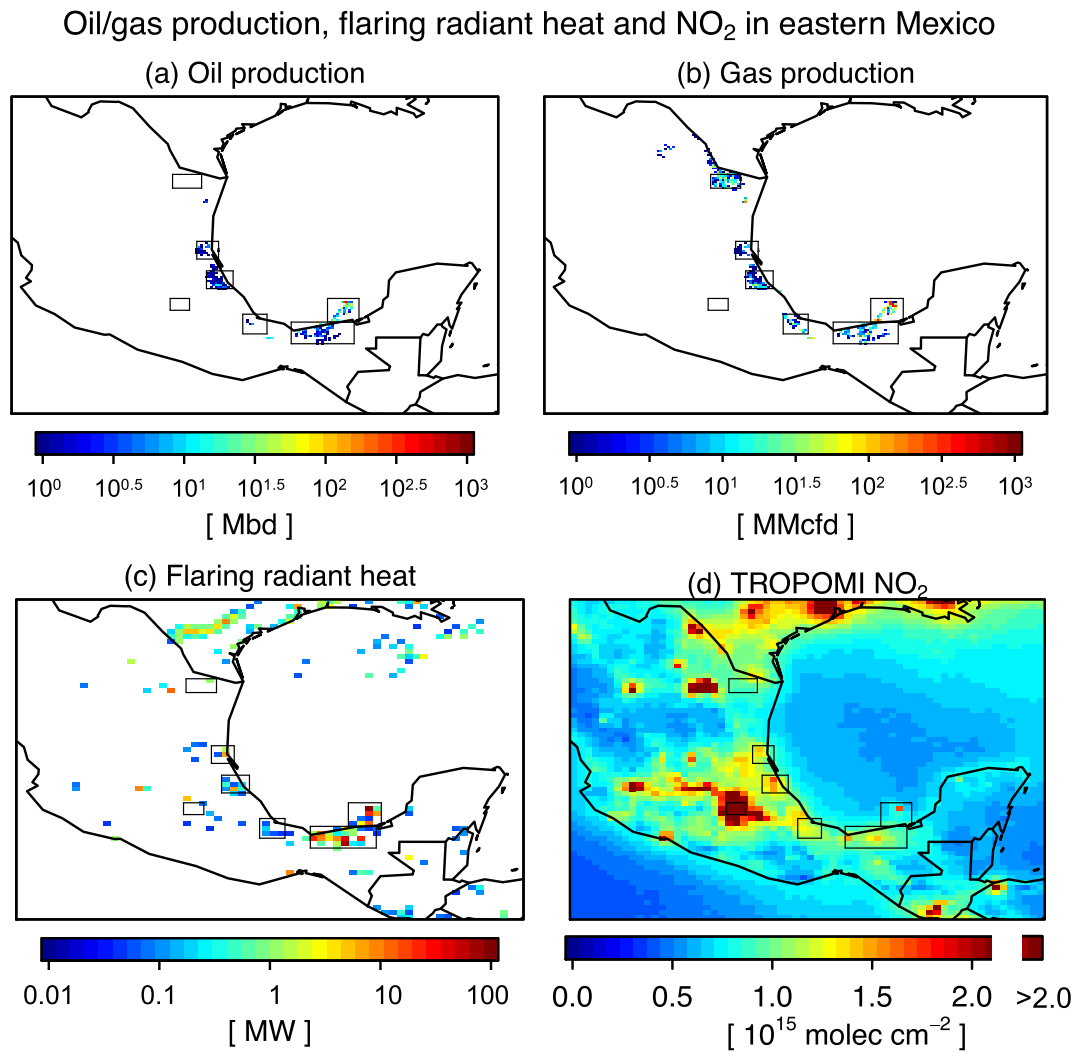
Oil/gas production, flaring radiant heat and NO$_2$ in eastern Mexico

(a) Oil production

(b) Gas production

(c) Flaring radiant heat

(d) TROPOMI NO$_2$

Fig. 2. Oil/gas production, flaring radiant heat, and TROPOMI NO$_2$ column mixing ratio in eastern Mexico (106°W-86°W, 14°N-30°N). (a) Oil production from the Hydrocarbon Information System (https://sih.hidrocarburos.gob.mx/, accessed in June 2020). The unit Mbd is thousand barrels per day. (b) Same as (a) but for gas production. The unit MMcfd is million cubic feet per day. (c) Gas flaring radiant heat (MW) from the Visible Infrared Imaging Radiometer Suite (VIIRS) data (Elvidge et al., 2015). (d) Tropospheric column density of NO$_2$ from TROPOMI. All data are averages for May 2018–December 2019 in eastern Mexico.

Posterior correction factors and DOFS in eastern Mexico

(a) Correction factors (posterior/prior)

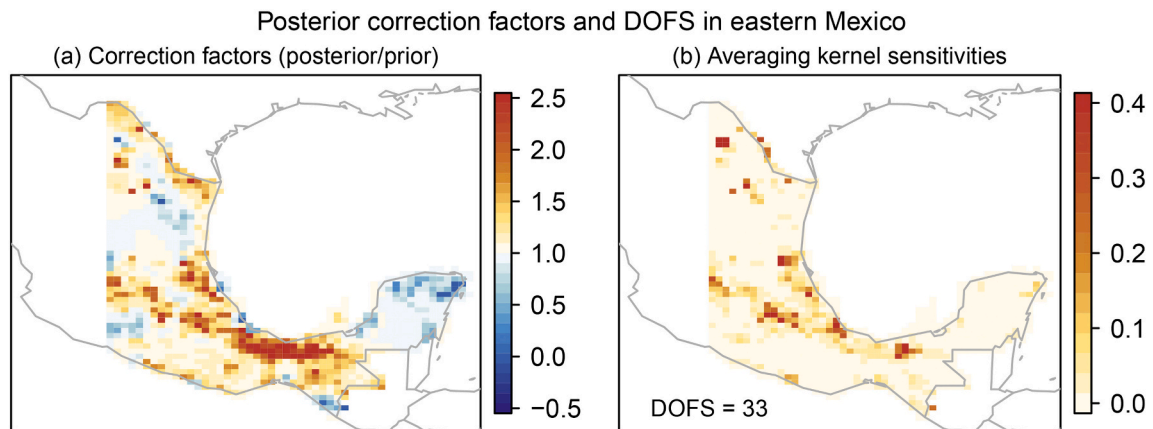### (b) Averaging kernel sensitivities

DOFS = 33

Fig. 3. Posterior correction factors and averaging kernel sensitivity in eastern Mexico. (a) TROPOMI data derived posterior correction factors using Bayesian inverse modeling. (b) Averaging kernel sensitivities representing the diagonal terms of the averaging kernel matrix.

emissions (Fig. 1 and S4). We find little sensitivity in Yucatan Peninsula (Southeastern Mexico) due to very few observations there (Fig. S1). The sensitivity is nearly zero in offshore gridcells with no TROPOMI data.

Fig. S9a compares the column-averaged methane in TROPOMI with GEOS-Chem simulations using prior estimates of methane emissions for gridcells with high averaging kernel sensitivity (>0.01) per gridcell in the inverse analysis. The prior simulation has a negative bias of 10–20 ppb across much of the eastern Mexico. GEOS-Chem simulations based posterior estimates indicate that the bias decreases to <5 ppb in coastal areas and < 10 ppb in Mexico City (Fig. S9b). This implies that our posterior solution can indeed provide improved forward model fit to observations, and the unresolved discrepancy may arise from the insufficient number of TROPOMI observations as implied by Fig. S1.

We attribute the posterior correction factors (E2) from the inversion to specific methane source sectors as described by E14. Based on E14, the posterior correction factor will be adjusted more for a specific sector if this sector has higher percentage in the total emissions and higher prior uncertainty. Fig. S10 displays the posterior correction factor for the oil/gas sector, which shows higher values in gridcells where the oil/gas emissions are the major source.

We also conduct an ensemble of inversions to test the robustness of our results to different assumptions in the inverse equations, including using different weighting of observations ($\gamma = 0.1, 0.25$ and 0.5) and prior estimates through bootstrapping (three scenarios of priors, see Methods for more details, Fig. S11-S13). Fig. 4a compares posterior emission totals with the prior ones for different sectors in eastern Mexico. We find most significant corrections are for the oil/gas sector, increasing from 0.55 Tg a^{-1} to 1.3 ± 0.2 Tg a^{-1} in eastern Mexico. Other

large corrections are for livestock and wetland. Our posterior estimates for eastern Mexico are 5.0 ± 0.2 Tg a^{-1} for anthropogenic sources and 1.5 ± 0.1 Tg a^{-1} for natural sources (details are provided in Table S2). The averaging kernel sensitivity computed following (Maasakkers et al., 2019) for the national emission estimate from each sector ranges from 0.6 to 1 (Table S2) for oil/gas, coal, landfill, and livestock sectors, suggesting the effectiveness of our inverse modeling framework involving TROPOMI data towards quantifying the total amount and the broader spatial distribution for these sectors in Mexico; but the sensitivity is much lower for other sectors because the emissions are smaller.

Fig. 4b further compares the prior and posterior emissions in the seven high-emitting oil and gas regions from the oil/gas sector. In the posterior estimates, these seven regions can account for ~80% of total oil/gas methane emissions in eastern Mexico. Specifically, we find a correction factor of >2 in R1, R3, R4 and R5. TROPOMI has no XCH$_4$ data over the ocean yet, therefore our inverse method has near-zero sensitivity in the offshore gridcells (Fig. 3b) and the posterior emissions remain almost unchanged (0.04 ± 0.01 Tg a^{-1}). The prior emissions in R5 are 0.23Tg a^{-1}, and our posterior estimates increase them to 0.74 ± 0.14 Tg a^{-1}, which accounts for 57% of total oil/gas emissions in eastern Mexico (more details are listed in Table S3). We also compare our emissions with the estimates from Zavala-Araiza et al. (2020) in a subdomain of R5 (Fig. S11). Our estimates for the R5 subdomain are 0.5 ± 0.1 Tg a^{-1}, compared to 0.21–0.30 Tg a^{-1} (95% CI) using aircraft measurements for two days in 2018 and 0.2–0.7 Tg a^{-1} (95% CI) by applying mass-balance methods to 2018–2019 TROPOMI observations in Zavala-Araiza et al. (2020). As a sensitivity test, we allowed a 25% error standard deviation in the uncertainty of the national bottom-up
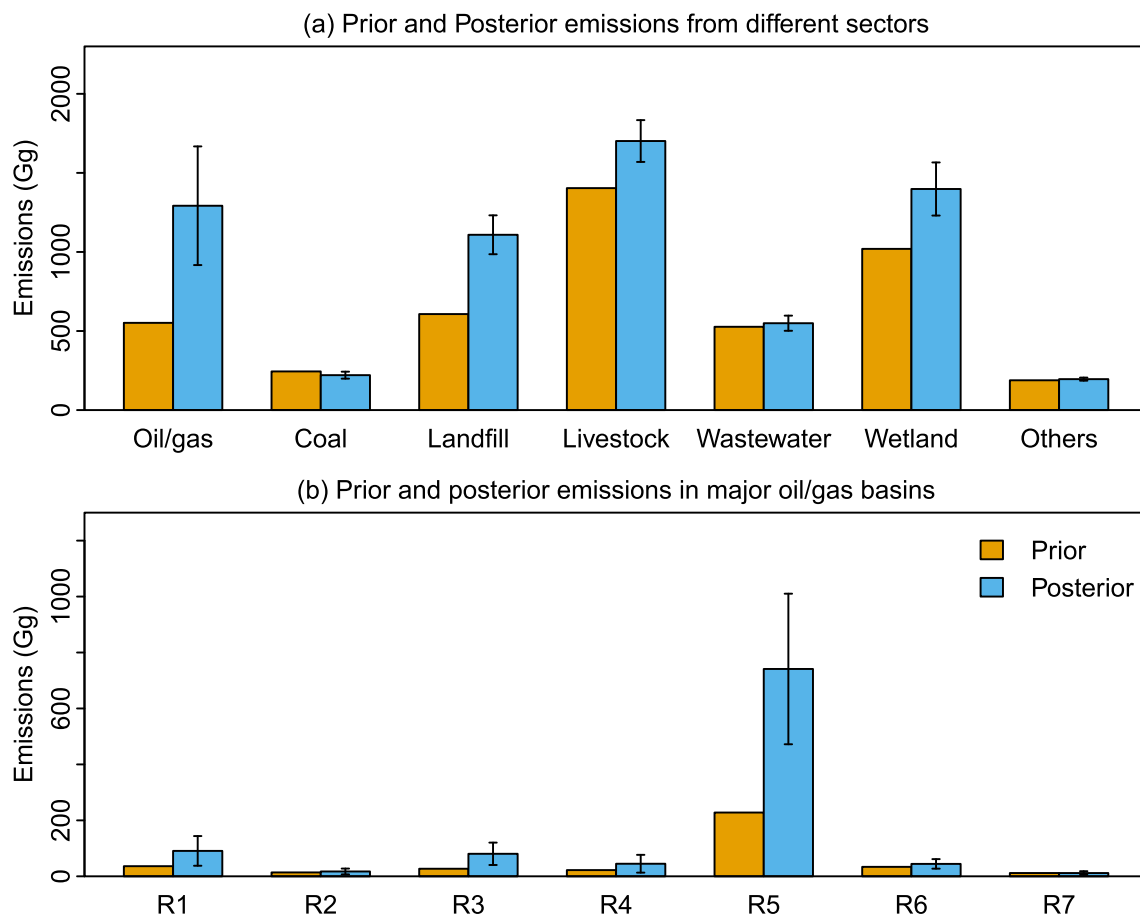

Fig. 4. Prior and posterior oil/gas emissions for different source sectors and high oil/gas emitting regions. (a) Annual mean prior and posterior methane emission in eastern Mexico for different sectors. The error bars denote the 95% confidence intervals (± 2σ), including uncertainty from both posterior errors and using different prior estimates and weighting of observations (γ). (b) Same as (a), but for the emissions from the oil/gas sector in 7 high-emitting regions.

inventory, showing little effect when compared to our central estimates (Fig. S14). This indicates our results are not sensitive to the choices of uncertainty of the bottom-up inventory.

Table S4 shows the flared methane emissions from prior estimates and calculated from VIIRS measurements (see Text S1 for method details). The percentage of flaring related emissions relative to the posterior emissions in the oil/gas sector based on the prior estimates is 50% in offshore gridcells (R6) and 14%–38% in onshore ones (R1-R5). Since the combustion efficiency is subject to large uncertainty, we calculate the flared methane from VIIRS data in three scenarios with high (98%), medium (90%) and low (84%) efficiency (INECC and SEMARNAT, 2018, see Methods for more details). In the high efficiency scenario, flared methane can account for one third of posterior emissions in R6 but less than 6% in onshore gridcells. These results indicate that flaring is a major source of emissions for the offshore region (R6) and that it is likely operated with a high combustion efficiency. Even in the less efficient combustion scenarios (which result in higher methane emissions), flaring still only accounts for <2% of posterior oil/gas emissions in R1 and R4, and 10–50% in R2, R3 and R5, much lower than the percentage from the prior estimates. These results for the onshore oil production regions (R2-R5) suggest that flaring doesn't seem to be the main driver of emissions, hinting at the existence of additional non-flaring related sources in onshore gridcells, especially for R5. Additional measurements that directly characterize flaring volumes and combustion efficiency are suggested as key next steps to further constrain emissions from this source (Caulton et al., 2014; Gvakharia et al., 2017; Zavala-Araiza et al., 2018).

Oil/gas emissions in the southern onshore basin (R5) account for more than half of total oil/gas emissions in the eastern Mexico domain. A number of factors may explain these potentially high non-flaring related sources in R5. First, the gas produced offshore (R6) is transported to onshore (R5) infrastructures and —as hypothesized by Zavala-Araiza et al. (2020)—is partially released to the atmosphere from the gathering and processing facilities within this region. In addition, Zhang et al. (2019) observed decreasing flared gas volume from offshore Mexico after 2008, which is in accordance with infrastructure investment (e.g. construction of new pipelines) to transport gas onshore aimed at reducing offshore flaring and venting (Romo, 2015). Given that the oil/gas production in R6 is 3–4 times higher than R5 (Table S1), this gas redistribution can easily increase the emissions in R5 (Fig. S15 and Table S1). Based on the satellite derived posterior emissions, the relative methane loss rate as normalized by gas production is 4.7% in eastern Mexico. The loss rate is in a moderately high range for R1-R4 (2%–6%), extremely high for R5 (13%) and low for R6 (0.4%). For reference, US average methane loss rate is approximately 2.3% (Alvarez et al., 2018) and loss rate for Permian basin in Texas is 3.7% (Zhang et al., 2020). The relative loss rate for R5 becomes 3%–5% if we assume 50%–100% gas produced in R6 is transported to R5. The calculation may support the assumption that R5 receives gas from R6 and help explain the relatively high emissions in R5 compared to all the other regions. These relatively high loss rates also suggest that oil/gas basins in Mexico have strong mitigation potential. Our second possible explanation for the large emissions is that most newly drilled wells from 2015 to 2019 are located in the southern onshore basin R5 (Fig. S15 and S16). It is plausible that a large fraction of the associated gas co-produced in R5 is vented to the atmosphere instead of flaring it or capturing it. Third, Zavala-Araiza et al. (2020) shows that processing plants in this region are large point sources (i.e., Nuevo Pemex and Cactus), and R5 has five processing plants while other basins have at most one (Table S5). The relatively high loss rates observed also suggest that there is a large opportunity to mitigate oil/gas related methane emissions in Mexico.

Further efforts could reduce the uncertainty of estimates of emissions estimates of this study. First, much of eastern Mexico has observations in <60 days of observations during this 20-month period (Fig. S1). Areas where lower sampling frequency exists reduces the capability of using TROPOMI to constrain the spatial distribution of emissions (Lorente

et al., 2020), which can be improved by using a longer period of observations after more data are acquired during the ongoing satellite observations in the coming years. Second, our study points to large non-flaring related emissions in R5, which should be further characterized with measurements at more granular scales. Ground-based and airborne-based measurements at the facility-level are needed to provide more in-depth information about the specific sources of high-emissions and therefore helping identify mitigation actions (Robertson et al., 2020; Johnson et al., 2017; Gorchov Negron et al., 2020). In addition, satellite observations with fine pixel resolution could also be useful in characterizing point sources (Cusworth et al., 2019; Varon et al., 2019). We suggest in depth field measurements, combined with high-resolution airborne/satellite surveys, are needed to provide a detailed emissions characterization of observed methane hotspots we report, and develop effective mitigation strategies.

4. Conclusions

Essentially all of Mexico's oil/gas production occurs in eastern Mexico with the region accounting for about 95% of methane emissions from the national oil/gas supply chain. However, bottom-up inventory-based estimates of emissions are very uncertain. In this study, we use 2018–2019 observations of column-averaged methane mixing ratio from TROPOMI to estimate methane emissions in eastern Mexico through an atmospheric inverse analysis at 0.25°x0.3125° horizontal resolution. Our work uses state-of-the-art emission inventories (Scarpelli et al., 2020) as prior estimates and also compare the emissions in the southern onshore and offshore basins to recent independent empirical estimates using aircraft measurements from Zavala-Araiza et al. (2020). Our posterior estimates for eastern Mexico are 5.0 ± 0.2 Tg a^{-1} for anthropogenic sources and 1.5 ± 0.1 Tg a^{-1} for natural sources. The posterior emissions from oil and natural gas production are scaled up by a factor of >2 and reach 1.3 ± 0.2 Tg a^{-1}, which accounts for a quarter of the anthropogenic emissions in eastern Mexico. This represents a loss rate of roughly 4.7% (methane emissions divided by gross natural gas production). Our posterior estimates show that 57% of the oil/gas emissions in eastern Mexico occurs in the southern onshore basin (0.79 $\pm$ 0.13 Tg a^{-1}), pointing at additional sources of high-emissions which are not represented in current bottom-up inventories (e.g., venting of associated gas, gathering/processing facilities emitting associated gas transported from offshore)—and require further characterization at a more granular scale. Overall, we find large discrepancy in oil/gas related methane emissions from Mexico, suggesting stronger measures are needed to effectively reduce emissions. Our work has demonstrated application of TROPOMI data in assessing the state of emissions on a national and regional basis as well as providing information on a sectoral basis.

Description of author's responsibilities

L. S., R. G., D. Z. A., M. O. and D. J. J. designed the experiments and L. S. carried them out., R. G., D. Z. A. and D.J.J. helped supervise the project. L. S. prepared the manuscript with contributions from all co-authors.

Code availability

TROPOMI data is can be accessed at http://www.tropomi.eu/data-products/methane. The forward model GEOS-Chem 12.7.0 can be downloaded at doi:https://doi.org/10.5281/zenodo.1343546. The code and data to reproduce figures in this work can be accessed from https://github.com/lshen2009/Shen_2020_Mexico.

Credit author statement

Lu Shen: Conceptualization, Methodology, Writing.

Daniel Zavala-Araiza: Conceptualization, Writing, Supervision.
Ritesh Gautam: Conceptualization, Writing, Supervision.
Mark Omara: Conceptualization, Writing, Reviewing and Editing.
Tia Scarpelli: Data, Reviewing and Editing.
Jianxiong Sheng: Reviewing and Editing.
Melissa P. Sulprizio: Model development, Reviewing and Editing.
Jiawei Zhuang: Model development, Reviewing and Editing.
Yuzhong Zhang: Reviewing and Editing.
Zhen Qu: Reviewing and Editing.
Xiao Lu: Reviewing and Editing.
Steven P. Hamburg: Reviewing and Editing.
Daniel J. Jacob: Conceptualization, Writing, Supervision.

Declaration of Competing Interest

The authors declare that they have no known competing financial interests or personal relationships.

that could have appeared to influence the work reported in this paper.

Acknowledgements

Appendix A. Supplementary data

Supplementary data to this article can be found online at https://doi.org/10.1016/j.rse.2021.112461.

References

Alvarez, R.A., Zavala-Araiza, D., Lyon, D.R., Allen, D.T., Barkley, Z.R., Brandt, A.R., Davis, K.J., Herndon, S.C., Jacob, D.J., Karion, A., Kort, E.A., 2018. Assessment of methane emissions from the US oil and gas supply chain. Science 361 (6398), 186–188. https://doi.org/10.1126/science.aar7204.

Bloom, A.A., Bowman, K.W., Lee, M., Turner, A.J., Schroeder, R., Worden, J.R., Weidner, R., McDonald, K.C., Jacob, D.J., 2017. A global wetland methane emissions and uncertainty dataset for atmospheric chemical transport models (WetCHARTs version 1.0). Geosci. Model Dev. 10, 2141–2156. https://doi.org/10.5194/gmd-10-2141-2017.

Brasseur, G.P., Jacob, D.J., 2017. Modeling of Atmospheric Chemistry. Cambridge University Press.

Butz, A., Guerlet, S., Hasekamp, O., Schepers, D., Galli, A., Aben, I., Frankenberg, C., Hartmann, J.M., Tran, H., Kuze, A., Keppel-Aleks, G., Toon, G., Wunch, D., Wennberg, P., Deutscher, N., Griffith, D., Macatangay, R., Messerschmidt, J., Notholt, J., Warneke, T., 2011. Toward accurate CO2 and CH4 observations from GOSAT. Geophys. Res. Lett. 38 https://doi.org/10.1029/2011gl047888 n/a-n/a.

Caulton, D.R., Shepson, P.B., Cambaliza, M.O., McCabe, D., Baum, E., Stirm, B.H., 2014. Methane destruction efficiency of natural gas flares associated with shale formation wells. Environ. Sci. Technol. 48 (16), 9548–9554. https://doi.org/10.1021/es500511w.

Crippa, M., Oreggioni, G., Guizzardi, D., Muntean, M., Schaaf, E., Lo Vullo, E., Solazzo, E., Monforti-Ferrario, F., Olivier, J.G.J., Vignati, E., 2019. Fossil CO2 and GHG Emissions of all World Countries - 2019 Report, EUR 29849 EN. Publications Office of the European Union, Luxembourg.

Cusworth, D.H., Jacob, D.J., Varon, D.J., Chan Miller, C., Liu, X., Chance, K., Thorpe, A. K., Duren, R.M., Miller, C.E., Thompson, D.R., Frankenberg, C., Guanter, L., Randles, C.A., 2019. Potential of next-generation imaging spectrometers to detect and quantify methane point sources from space. Atmos. Meas. Tech. 12, 5655–5668. https://doi.org/10.5194/amt-12-5655-2019.

de Gouw, J.A., Veefkind, J.P., Roosenbrand, E., Dix, B., Lin, J.C., Landgraf, J., Levelt, P. F., 2020. Daily satellite observations of methane from oil and gas production regions in the United States. Sci. Rep. 10, 1379. https://doi.org/10.1038/s41598-020-57678-4.

Duncan, B.N., Lamsal, L.N., Thompson, A.M., Yoshida, Y., Lu, Z., Streets, D.G., Hurwitz, M.M., Pickering, K.E., 2016. A space-based, high-resolution view of notable changes in urban NOx pollution around the world (2005–2014). J. Geophys. Res. Atmos. 121, 976–996. https://doi.org/10.1002/2015JD024121.

Elvidge, C.D., Zhizhin, M., Baugh, K., Hsu, F.C., Ghosh, T., 2016. Methods for global survey of natural gas flaring from visible infrared imaging radiometer suite data. Energies 9 (1), 14. https://doi.org/10.3390/en9010014.

Gorchov Negron, A.M., Kort, E.A., Conley, S.A., Smith, M.L., 2020. Airborne assessment of methane emissions from offshore platforms in the U.S Gulf of Mexico. Environ. Sci. Technol. 54, 5112–5120. https://doi.org/10.1021/acs.est.0c00179.

Gvakharia, A., Kort, E.A., Brandt, A., Peischl, J., Ryerson, T.B., Schwarz, J.P., Smith, M. L., Sweeney, C., 2017. Methane, black carbon, and ethane emissions from natural gas flares in the Bakken Shale, North Dakota. Environ. Sci. Technol. 51, 5317–5325. https://doi.org/10.1021/acs.est.6b05183.

Hasekamp, O., Lorente, A., Hu, H., Butz, A., de Brugh, J., Landgraf, J., 2019. Algorithm Theoretical Baseline Document for Sentinel-5 Precursor Methane Retrieval, 67. Netherlands Institute for Space Research available at: http://www.tropomi.eu/sites/default/files/files/publicSentinel-5P-TROPOMI-ATBD-Methane-retrieval.pdf.

Heald, C.L., Jacob, D.J., Jones, D.B.A., Palmer, P.I., Logan, J.A., Streets, D.G., Sachse, G. W., Gille, J.C., Hoffman, R.N., Nehrkorn, T., 2004. Comparative inverse analysis of satellite (MOPITT) and aircraft (TRACE-P) observations to estimate Asian sources of carbon monoxide. J. Geophys. Res. 109 https://doi.org/10.1029/2004jd005185.

Hu, H., Hasekamp, O., Butz, A., Galli, A., Landgraf, J., de Brugh, J.A., Borsdorff, T., Scheepmaker, R., Aben, I., 2016. The operational methane retrieval algorithm for TROPOMI. Atmosp. Measur. Techn. 9, 5423–5440. https://doi.org/10.5194/amt-9-5423-2016.

IMP, 2012. Determinacion de factores de emision para emisiones fugitivas de la industria petrolera en Mexico. https://www.gob.mx/cms/uploads/attachment/file/167851/emisiones_fugitivas.pdf.

INECC and SEMARNAT, 2018. M'exico: Inventario Nacional de Emisiones de Gases y Compuesto de Efecto Invernadero 1990–2015 (INEGyCEI). Instituto Nacional de Ecología y Cambio Clim'atico (INECC) and Secretaría de Medio Ambiente y Recursos Naturales (SEMARNAT).

IPCC, 2013. Summary for policymakers. In: Stocker, T.F., Qin, D., Plattner, G.-K., Tignor, M., Allen, S.K., Boschung, J., Midgley, P.M. (Eds.), Climate Change 2013: The Physical Science Basis. Contribution of Working Group I to the Fifth Assessment Report of the Intergovernmental Panel on Climate Change. Cambridge University Press, Cambridge, UK and New York, NY, USA, pp. 3–29.

Janssens-Maenhout, G., Crippa, M., Guizzardi, D., Muntean, M., Schaaf, E., Dentener, F., Bergamaschi, P., Pagliari, V., Olivier, J.G.J., Peters, J.A.H.W., van Aardenne, J.A., Monni, S., Doering, U., Petrescu, A.M.R., Solazzo, E., Oreggioni, G.D., 2019. EDGAR v4.3.2 global atlas of the three major greenhouse gas emissions for the period 1970–2012. Earth Syst. Sci. Data 11, 959–1002. https://doi.org/10.5194/essd-11-959-2019.

Johnson, M.R., Tyner, D.R., Conley, S., Schwietzke, S., Zavala-Araiza, D., 2017. Comparisons of airborne measurements and inventory estimates of methane emissions in the Alberta upstream oil and gas sector. Environ. Sci. Technol. 51, 13008–13017. https://doi.org/10.1021/acs.est.7b03525.

Kort, E.A., Frankenberg, C., Costigan, K.R., Lindenmaier, R., Dubey, M.K., Wunch, D., 2014. Four corners: the largest US methane anomaly viewed from space. Geophys. Res. Lett. 41 https://doi.org/10.1002/2014gl061503.

Lorente, A., Borsdorff, T., Butz, A., Hasekamp, O., de Brugh, J., Schneider, A., Hase, F., Kivi, R., Wunch, D., Pollard, D.F., Shiomi, K., Deutscher, N.M., Velazco, V.A., Roehl, C.M., Wennberg, P.O., Warneke, T., Landgraf, J., 2020. Methane retrieved from TROPOMI: improvement of the data product and validation of the first two years of measurements. Atmos. Meas. Tech. Discuss. https://doi.org/10.5194/amt-2020-281.

Lucchesi, R., 2013. File specification for GEOS-5 FP. In: GMAO Office Note No. 4 (Version 1.0), 63 pp, available from. http://gmao.gsfc.nasa.gov/pubs/office_notes.

Maasakkers, J.D., Jacob, D.J., Sulprizio, M.P., Turner, A.J., Weitz, M., Wirth, T., Hight, C., DeFigueiredo, M., Desai, M., Schmeltz, R., Hockstad, L., Bloom, A.A., Bowman, K.W., Jeong, S., Fischer, M.L., 2016. Gridded National Inventory of U.S. methane emissions. Environ. Sci. Technol. 50, 13123–13133. https://doi.org/10.1021/acs.est.6b02878.

Maasakkers, J.D., Jacob, D.J., Sulprizio, M.P., Scarpelli, T.R., Nesser, H., Sheng, J.-X., Zhang, Y., Hersher, M., Bloom, A.A., Bowman, K.W., Worden, J.R., Janssens-Maenhout, G., Parker, R.J., 2019. Global distribution of methane emissions, emission trends, and OH concentrations and trends inferred from an inversion of GOSAT satellite data for 2010–2015. Atmos. Chem. Phys. 19, 7859–7881. https://doi.org/10.5194/acp-19-7859-2019.

Myhre, G., Shindell, D., Bréon, F.-M., Collins, W., Fuglestvedt, J., Huang, J., Koch, D., Lamarque, J.-F., Lee, D., Mendoza, B., Nakajima, T., Robock, A., Stephens, G., Takemura, T., Zhang, H., Anthropogenic and Natural Radiative Forcing, in: Climate Change 2013, 2013. In: Stocker, T.F., Qin, D., Plattner, G.-K., Tignor, M., Allen, S.K., Boschung, J., Midgley, P.M. (Eds.), The Physical Science Basis. Contribution of Working Group I to the Fifth Assessment Report of the Inter- governmental Panel on Climate Change. Cambridge University Press, Cambridge, United Kingdom and New York, NY, USA.

Pandey, S., Gautam, R., Houweling, S., van der Gon, H.D., Sadavarte, P., Borsdorff, T., Hasekamp, O., Landgraf, J., Tol, P., van Kempen, T., Hoogeveen, R., van Hees, R., Hamburg, S.P., Maasakkers, J.D., Aben, I., 2019. Satellite observations reveal extreme methane leakage from a natural gas well blowout. P. Natl. Acad. Sci. USA 116, 26376–26381. https://doi.org/10.1073/pnas.1908712116.

Parker, R.J., Webb, A., Boesch, H., Somkuti, P., Barrio Guillo, R., Di Noia, A., Kalaitzi, N., Anand, J.S., Bergamaschi, P., Chevallier, F., Palmer, P.I., Feng, L., Deutscher, N.M., Feist, D.G., Griffith, D.W.T., Hase, F., Kivi, R., Morino, I., Notholt, J., Oh, Y.-S., Ohyama, H., Petri, C., Pollard, D.F., Roehl, C., Sha, M.K., Shiomi, K., Strong, K., Sussmann, R., Té, Y., Velazco, V.A., Warneke, T., Wennberg, P.O., Wunch, D., 2020.

A decade of GOSAT Proxy satellite CH4 observations. Earth Syst. Sci. Data 12, 3383–3412. https://doi.org/10.5194/essd-12-3383-2020.

Robertson, A.M., Edie, R., Field, R.A., Lyon, D., McVay, R., Omara, M., Zavala-Araiza, D., Murphy, S.M., 2020. New Mexico Permian Basin measured well pad methane emissions are a factor of 5–9 times higher than US EPA estimates. Environ. Sci. Technol. 54 (21), 13926–13934. https://doi.org/10.1021/acs.est.0c02927.

Romo, D., 2015. The Cantarell oil field and the Mexican economy. Develop. Prob. 46 (183), 141–164.

Scarpelli, T.R., Jacob, D.J., Villasana, C.A.O., Hernández, I.F.R., Moreno, P.R.C., Alfaro, E.A.C., García, M.Á.G., Zavala-Araiza, D., 2020. A gridded inventory of anthropogenic methane emissions from Mexico based on Mexico's national inventory of greenhouse gases and compounds. Environ. Res. Lett. 15, 105015. https://doi.org/10.1088/1748-9326/abb42b.

Schneising, O., Buchwitz, M., Reuter, M., Vanselow, S., Bovensmann, H., Burrows, J.P., 2020. Remote sensing of methane leakage from natural gas and petroleum systems revisited. Atmos. Chem. Phys. 20, 9169–9182. https://doi.org/10.5194/acp-20-9169-2020.

SEMARNAT, 2012. Mexico quinta comunicacion nacional ante la Convencion Marco de las Naciones Unidas sobre el Cambio Climatico.

Sheng, J.-X., Jacob, D.J., Maasakkers, J.D., Sulprizio, M.P., Zavala-Araiza, D., Hamburg, S.P., 2017. A high-resolution (0.1°×0.1°) inventory of methane emissions from Canadian and Mexican oil and gas systems. Atmos. Environ. 158, 211–215. https://doi.org/10.1016/j.atmosenv.2017.02.036.

Smith, J., Shah, T., Parker, L., Grant, J., Yarwood, G., 2018. Modeling Inventories for Mexico and Caribbean Countries to Support Quantitative Analysis of International Transport Impacts on Ozone Design Values and Regional Haze Final Report.

Varon, D.J., McKeever, J., Jervis, D., Maasakkers, J.D., Pandey, S., Houweling, S., et al., 2019. Satellite discovery of anomalously large methane point sources from oil/gas production. Geophys. Res. Lett. 46, 13,507–13,516. https://doi.org/10.1029/2019GL083798.

Veefkind, J.P., Aben, I., McMullan, K., Förster, H., de Vries, J., Otter, G., et al., 2012. TROPOMI on the ESA Sentinel-5 precursor: a GMES mission for global observations of the atmospheric composition for climate, air quality and ozone layer applications. Remote Sens. Environ. 120, 70–83. https://doi.org/10.1016/j.rse.2011.09.027.

Wecht, K.J., Jacob, D.J., Frankenberg, C., Jiang, Z., Blake, D.R., 2014. Mapping of north American methane emissions with high spatial resolution by inversion of SCIAMACHY satellite data. J. Geophys. Res. 119, 7741–7756. https://doi.org/10.1002/2014jd021551.

Zavala-Araiza, D., Herndon, S.C., Roscioli, J.R., Yacovitch, T.I., Johnson, M.R., Tyner, D. R., Omara, M., Knighton, B., 2018. Methane emissions from oil and gas production sites in Alberta, Canada. Elem Sci Anth 6 (27), 3–13.

Zavala-Araiza, D., Omara, M., Gautam, R., Smith, M.L., et al., 2020. A tale of two regions: methane emissions from oil and gas production in offshore/onshore Mexico. Environ. Res. Lett. 16, 024019.

Zhang, Y., Gautam, R., Zavala-Araiza, D., Jacob, D.J., Zhang, R., Zhu, L., Sheng, J.-X., Scarpelli, T., 2019. Satellite-observed changes in Mexico's offshore gas flaring activity linked to oil/gas regulations. Geophys. Res. Lett. 46, 1879–1888. https://doi.org/10.1029/2018GL081145.

Zhang, Y., Gautam, R., Pandey, S., Omara, M., Maasakkers, J.D., Sadavarte, P., Lyon, D., Nesser, H., Sulprizio, M.P., Varon, D.J., Zhang, R., 2020. Quantifying methane emissions from the largest oil-producing basin in the United States from space. Sci. Adv. 6 (17) https://doi.org/10.1126/sciadv.aaz5120 eaaz5120.